ACS MATERIALS LETTERS

www.acsmaterialsletters.org

# Converging Hydrogen-Bonded Water Transport Channel with External Magnetic Field in a Janus Molecular Cobalt Phosphate for Enhanced Oxygen Evolution Reaction (OER) Activity

*Published as part of ACS Materials Letters virtual special issue "Materials for Water Splitting".*

Tulasi Prapakaran, Ananya Chowdhury,[∇] Sunita Sharma,[∇] Itisha Dwivedi, Gopalan Rajaraman,[*] Chandramouli Subramaniam,[*] and Ramaswamy Murugavel[*]

Cite This: *ACS Materials Lett.* 2024, 6, 2126−2135

Read Online

ACCESS | Metrics & More | Article Recommendations | Supporting Information

**ABSTRACT:** **Increasing the water content and the hydrophobic accessibility through hydrogen-bonded dimeric cavities of Janus-faced mononuclear Co(II) phosphates, pristine complex [Co(Cl-tpy)-(dtbppH)$_2$(H$_2$O)]·(H$_2$O)(2MeOH) (1-xtal), and sonicated [Co(Cl-tpy)(dtbppH)$_2$(H$_2$O)]·(H$_2$O)$_n$ (1-soni) produces systematic increments in the anodic water-splitting reaction (OER), which is further enhanced by an external magnetic field (50−300 mT), with water-rich 1-soni exhibiting the best electrocatalytic activity and energy efficiency. Such enhanced catalytic activity is traced to spin-state switching of a key intermediate formed during the catalytic cycle, offering a lower kinetic barrier from denisty functional theory calculations. Since the energy gap between these spin states is small, this suggests preferential switching of state with a lower kinetic barrier in the presence of a magnetic field, rationalizing the observed behavior.**

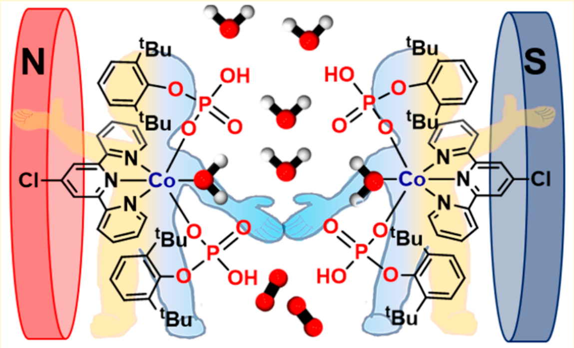

Green hydrogen, produced via electrochemical water splitting using solar or wind power, is a renewable energy vector that holds the potential to substitute for carbon-based fuels in transportation and mobility applications. Moreover, it is a feedstock for the chemical industry, which still mainly uses gray hydrogen produced from reforming natural gas or gasification of coal.[1] Water electrolysis (splitting) consists of the cathodic hydrogen evolution reaction (HER) and the anodic oxygen evolution reaction (OER). However, the bottleneck in boosting water electrolysis technologies is the sluggish oxygen evolution process, which significantly hampers the overall efficiency of water splitting.[2−4] At present, the state-of-the-art electrocatalyst for the OER is a material based on IrO$_2$/RuO$_2$. However, the high cost and scarcity of these catalysts severely impede their wide applications.[5,6] Consequently, developing efficient water-oxidation catalysts using Earth-abundant transition metals (phosphates, oxides, hydroxides, perovskites, nitrides, and chalcogenides) have recently witnessed substantial advancements.[7−14]

Transition-metal-based molecular electrocatalysts are promising in achieving high specific catalytic activity and selectivity.[15−18] Among them, cobalt has emerged as an interesting non-noble-metal molecular catalyst for water splitting.[18−23] We have recently shown that an organo-soluble Co-phosphate polymer can be hybridized with hard carbon to produce some of the best Co-based OER catalysts.[24−26] More recently, a cobalt phosphate tetranuclear cluster has been shown to perform overall water splitting with a full-cell overpotential of 0.94 V, if the primary coordination environ-

Received: April 8, 2024
Revised: April 25, 2024
Accepted: April 25, 2024

https://doi.org/10.1021/acsmaterialslett.4c00763

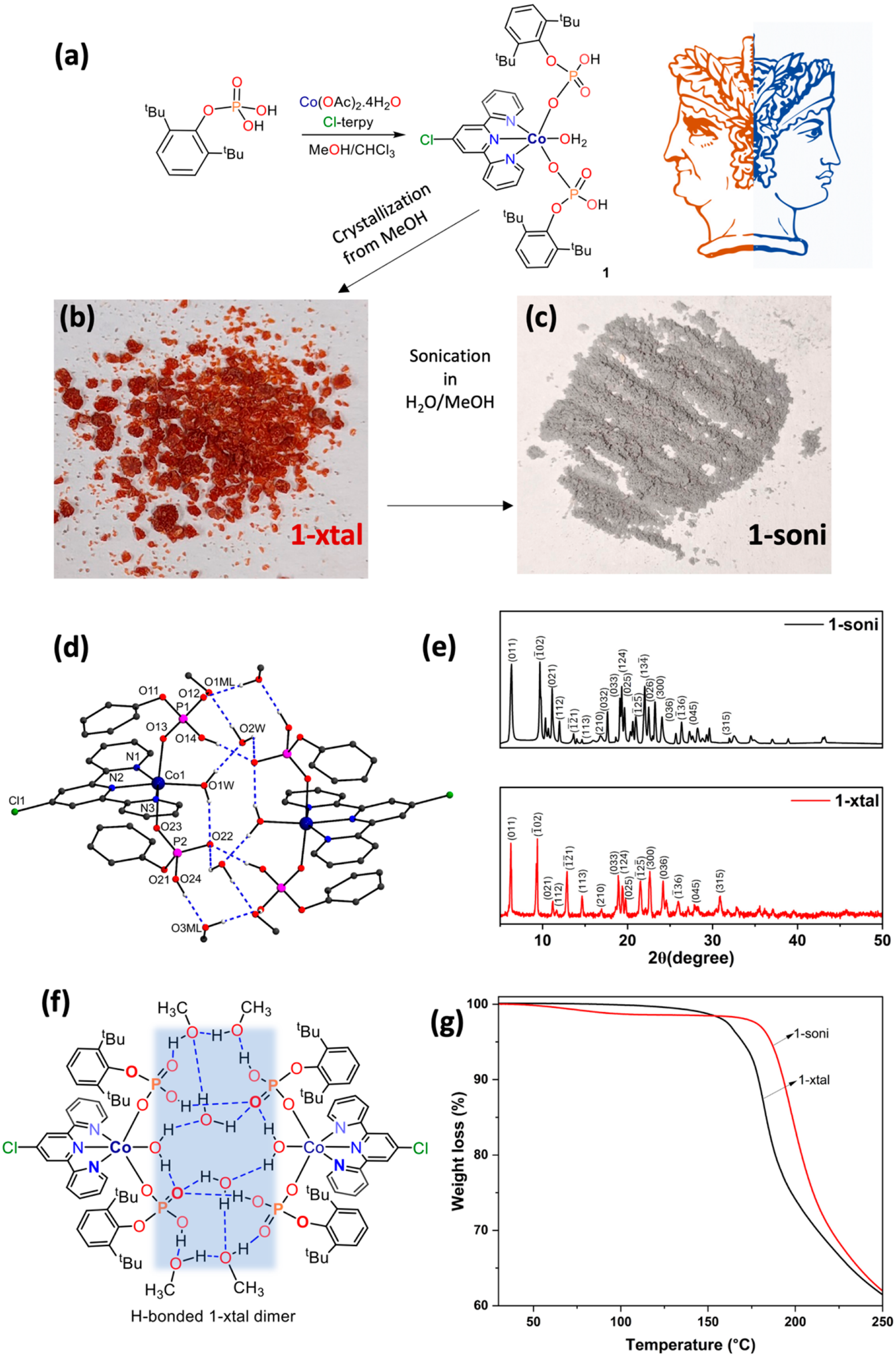

**Figure 1.** (a) Synthesis of Janus cobalt catalyst 1, (b) single crystals of 1-xtal grown from methanol; (c) ultrasonicated sample of 1-xtal showing significant color change (1-soni); (d) crystal structure of 1-xtal showing hydrogen-bonded dimer formation assisted by lattice water and methanol molecules, forming a hydrophilic channel; (e) powder X-ray diffractogram; (f) schematic representation of the dimeric structure revealing water transport channel (blue shaded area); and (g) thermogravimetric profiles of 1-xtal and 1-soni.

ment is suitably modulated both in terms of coordination number and geometry.[27]

Besides, control and manipulation of structure can be precisely implemented at the first and second coordination spheres of such molecular catalysts.[28,29] These subtle variations provide mechanistic insights into the structural impacts on the geometric and electronic configurations of active sites of the molecular catalyst, which is comparatively systematic and distinct from insights gleaned from studies of bulk or nanosized metal catalysts focusing on their surfaces and interfaces.[30] Furthermore, the molecular catalysts can be studied heterogeneously by immobilizing onto solid supports or adsorption/grafting to an electrode.[27,31] The heterogenized molecular catalysts are usually suitable for integrating into the devices for practical applications.[31−35]

Designing a catalyst with an idealized active center, geometry, and electronic properties can enhance its catalytic activity.[14] However, recent studies indicate that the spin states of the catalytic centers can also influence the activity.[36] Specifically, spin configurations at the interface between the catalyst and the adsorbate play a crucial role in the OER. This reaction involves the conversion of diamagnetic species (hydroxy or water) to paramagnetic oxygen molecules (spin-forbidden process). Consequently, additional energy is necessary to facilitate the reaction, potentially contributing to the high OER overpotential.[37,38] Recent studies indicate that spin polarization in magnetic catalysts subjected to external magnetic field can lower electron transfer barriers and enhance OER efficiency.[36] Although the impact of magnetic fields on catalysis has been investigated for several decades, these benefits have traditionally been attributed to indirect effects,[39−41] neglecting the significance of spin-based mechanisms in magnetic catalysis. After Gracia's prediction on the spin dependence of electrocatalytic water splitting,[37,38] extensive focus has been placed on integrating the experimental aspects of spin states and spin polarization effects in magnetic catalysis. While most research focuses on OER enhancement emanating from ferromagnetic bulk catalysts,[42−44] only a few studies have focused on such effects at the molecular/atomic scale.[45,46] In this context, coordination complexes are highly suitable for investigating spin effects in contrast to single metal atoms, because of their tunable crystal fields and orbital occupancies.[47] Hence, developing stable and heterogeneous molecular catalysts and augmenting their efficiency through spin regulation using an external magnetic field can open up new opportunities in oxygen electrocatalysis.

Given the aforementioned background, in the present study, we describe a mononuclear cobalt complex $[Co(tpy)(dtbppH)_2(H_2O)]\cdot H_2O(2MeOH)$, in which the redox active Co(II) center is placed in an environment that is amenable for activation of water inside the primary coordination sphere. This unique chemical environment is further leveraged through an external magnetic field driven spin-state dynamics, resulting in enhanced OER kinetics. This study particularly derives inspiration from our earlier demonstrated strategy of flanking coordinated water molecule between two phosphoryl oxygens on a five-coordinated copper phosphate (Scheme S1).[48]

Reaction of $Co(OAc)_2\cdot 4H_2O$ with 2,6-di-*tert*-butylphenyl phosphate ($dtbppH_2$) and Cl-tpy in $MeOH/CHCl_3$ yields the $[Co(Cl\text{-}tpy)(dtbppH)_2(H_2O)]\cdot(H_2O)(2MeOH)$ (**1-xtal**, see Figure 1). Ultrasonication of **1-xtal** for 30 min in a methanol/water mixture results in the breakdown of crystals into a fine powder, which is accompanied by a color change from orange (**1-xtal**) to pale purple (**1-soni**) (Figures 1b and 1c). This is further confirmed from the solid-state diffuse reflectance spectra that exhibit a distinct shoulder at 360 nm for **1-soni**, suggesting a change in its coordination environment during sonication (Figure S1). Further evidence from SEM and TEM images shows clear downsizing of **1-xtal** upon sonication (Figures S2−S4). The Fourier transform infrared (FT-IR) spectrum of **1-xtal** and **1-soni** exhibit a broad absorption band at ~3408 and 3407 $cm^{-1}$ for the water −OH group and a broad absorption at 2375 and 2355 $cm^{-1}$ for the residual P−OH group, respectively (Figure S5).[49] Correspondingly, the Raman vibrational modes **1-xtal** and **1-soni** appear at 1004 and 670 $cm^{-1}$ and arise due to the triply degenerate antisymmetric stretching vibrations of the phosphate ligands and the presence of the Co(II) ions (Figure S6).[49,50]

In the monomeric Co(II) complex (Table S1), the metal ion is surrounded by a tridentate Cl-tpy, two mono deprotonated phosphate ligands, and a coordinated water molecule, resulting in hexa-coordinated Co(II) center (Figure 1d). The SHAPE analysis reveals that Co(II) ion in the structure displays a near octahedral symmetry (Table S2).[51] Three N atoms from the chelating Cl-tpy ligand (N1−N3) and the aqua ligand occupy the equatorial positions, while the axial coordination sites are occupied by phosphate O atoms from two different dtbppH ligands. In other words, the water oxygen is coordinated to the metal in the same plane as that of the N3Co plane, while the two phosphate O atoms coordinate orthogonally in opposite directions. The average bond lengths of Co−N (2.135 Å), (P)O−Co (2.082 Å), and Co−O (2.057 Å) in **1-xtal** are comparable to those of similar cobalt phosphate complexes.[52] Strong hydrogen-bonding interactions occur between the protons of the coordinated water molecule (OW1) and the O atom of the lattice water molecule (O2W) and the phosphoryl O atom of the coordinated phosphate molecule (O22). Furthermore, the free P−OH groups and phosphoryl oxygens (P═O) of coordinated dtbppH ligands and lattice MeOH are also bonded to each other through H-bridges. This pattern of the hydrogen bonding leads to the formation of a hydrogen-bonded dimeric structure involving four lattice methanol molecules, two lattice water molecules, two coordinated water molecules, and four of each the P═O groups and P−OH groups of the coordinated phosphate ligands, as shown in Figure 1f and Figure S7 (Table S3).

Experimental and simulated PXRD patterns of **1-xtal** exhibit good agreement, suggesting its phase purity (Figure S8). Moreover, the PXRD of **1-soni** exhibits minor line broadening indicating partial loss of crystallinity due to sonication and possible water incorporation in the lattice (Figure 1e and Figure S8).[53,54] The CHN and thermogravimetric analyses provide evidence for the presence of additional water molecules in the crystal lattice (Table S4). The initial weight loss of 10.02% (10.3%) at 180 °C in **1-xtal** accounts for the removal of coordinated and lattice solvent molecules. In comparison, **1-soni** exhibits an initial weight loss from the removal of additional lattice water molecule, with a calculated value of ~1.77% (found value: 1.8%) at 97 °C. Subsequent loss of two molecules of water and methanol each (calc., 9.84%; found, 10.2%) at 190 °C. Further confirmation for the presence of additional water molecules in **1-soni** is obtained from mass spectra of the evolved gases during thermogravimetry (Figure S9). The XPS studies described vide infra further support these observations. The room-temperature magnetic susceptibilities ($\chi_{MT}$) of **1-xtal** and **1-soni** are 3.22 and 3.47 $cm^3$ K $mol^{-1}$, respectively (Figure S10). These values correspond to the spin ground state of $S = {}^3/_2$ (the spin-only value is 1.875 $cm^3$ K $mol^{-1}$). The susceptibility decreases below 100 K, suggesting the presence of strong anisotropy, as expected for a distorted mononuclear octahedral Co(II) complex (Figure S10).

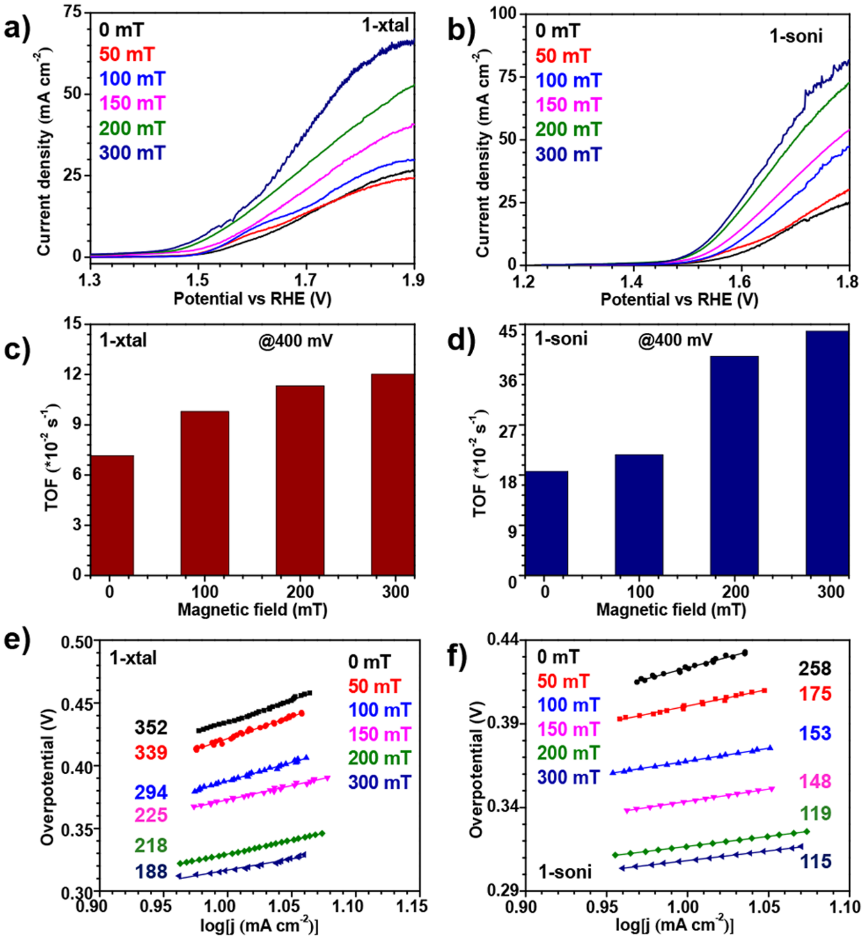

**Figure 2. LSV curves for (a) 1-xtal and (b) 1-soni, at varying magnetic field (0−300 mT). The corresponding turnover frequencies (TOF), estimated from the Co-OOH feature, are shown in panels (c) and (d), respectively. The Tafel slopes (in mV/dec) for 1-xtal and 1-soni, establishing a systematic variation with magnetic field, are presented in panels (e) and (f), respectively.**

The Janus-faced **1-xtal** thereby forms a directed channel (Figure 1f) that facilitates the movement of water and simultaneously provides direct access to the Co(II) ion catalytic site. Furthermore, the ultrasonic perturbation of **1-xtal** in a water/methanol mixture leads to the formation of **1-soni**, which is more conducive to water oxidation. Thus, **1-xtal** and its crafted variant **1-soni** serve as model systems to highlight the importance of (a) incorporating molecular passages to facilitate the continuous flux of water to the electroactive Co(II) ion site and (b) leveraging the intrinsic magnetism of molecular catalysts to effect magneto-electrocatalytic enhancements in the OER. The latter goal aims to synergize the two major disciplines of molecular magnetism with energy-efficient electrocatalysis and is attempted on molecularly designed heterogeneous catalysts for the first time, to the best of our knowledge.

The heterogeneous electrocatalytic OER activity of **1-xtal** and **1-soni** were investigated by drop-casting these samples (0.4 mg/cm$^2$) on clean glassy carbon electrodes (diameter = 3 mm) (Figure 2). While the immediate coordination environment around Co(II) is the same in both **1-xtal** and **1-soni**, changes in their secondary coordination environment are reflected in their OER catalytic activity. The formation of the Co-OOH intermediate that accompanies the Co$^{2+}$−Co$^{3+}$ oxidation is evident from the peak at 1.47 V for both the catalysts, signifying their propensity for water coordination (Figure S11).[55] Furthermore, the OER onset potentials and overpotentials are marginally lower for **1-soni** (365 mV, 418 mV@10 mA/cm$^2$) compared to **1-xtal** (384 mV, 444 mV@10 mA/cm$^2$), giving a clear indication of the accessibility of the catalytic site mediated through the secondary coordination environment (Figures 2a and 2b, Table 1). Interestingly, such minor variations in the electrochemical potentials manifest as significant changes in their Tafel slopes, with **1-soni** exhibiting a significantly larger kinetic facility (258 mV/dec), compared to **1-xtal** (352 mV/dec) (Figures 2e and 2f, and Table 1). Such

**Table 1. Comparison of the Overpotential, Onset Potential, and Tafel Slope of the OER Electrocatalytic Parameters for 1-xtal and 1-soni under Varying Conditions of an External Magnetic Field**

| | 1-xtal | | | 1-soni | | |
|---|---|---|---|---|---|---|
| applied magnetic field (mT) | $\eta^{\text{onset}}$ (mV) | $\eta^{10}$ (mV) | Tafel slope (mV/dec) | $\eta^{\text{onset}}$ (mV) | $\eta^{10}$ (mV) | Tafel slope (mV/dec) |
| 0 | 384 | 444 | 352 | 365 | 418 | 258 |
| 50 | 363 | 418 | 339 | 352 | 398 | 175 |
| 100 | 320 | 386 | 294 | 308 | 367 | 153 |
| 150 | 296 | 362 | 225 | 280 | 343 | 148 |
| 200 | 277 | 339 | 218 | 257 | 316 | 119 |
| 300 | 262 | 329 | 188 | 243 | 306 | 115 |

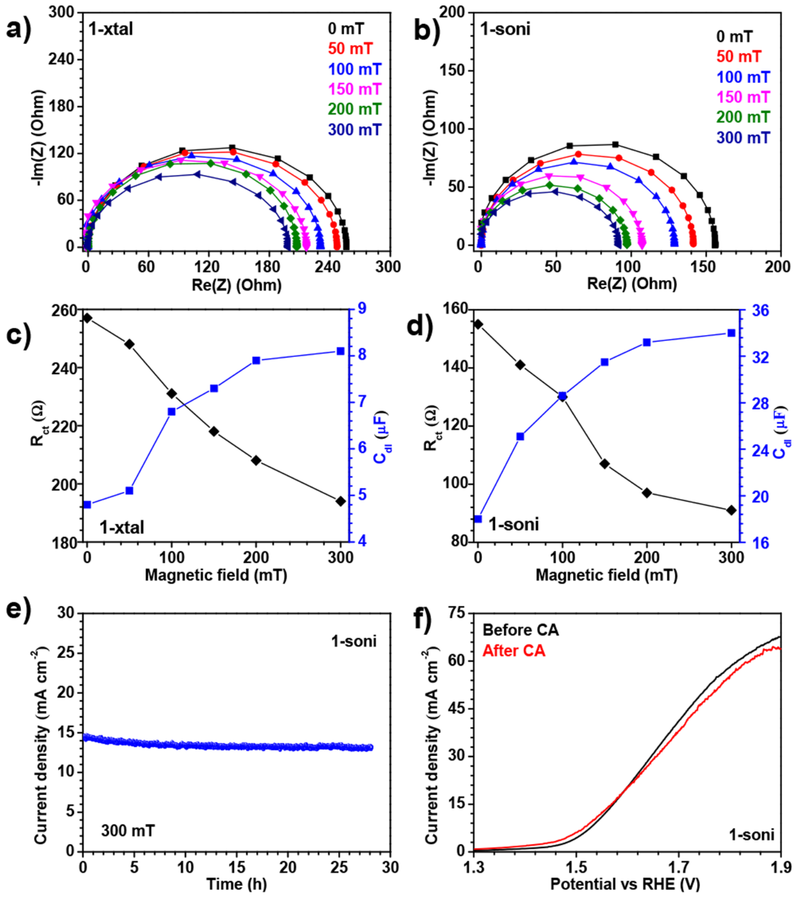

**Figure 3. Nyquist plots for (a) 1-xtal and (b) 1-soni at varying magnetic field (0−300 mT). Variation of $R_{ct}$ and $C_{dl}$ for the (c) 1-xtal and (d) 1-soni catalysts. Chronoamperometric plots of OER activity with (e) 1-soni, recorded at 300 mT, for 28 h and (f) LSV indicating its structural and chemical integrity after catalysis.**

significant differences in the Tafel slope, albeit for a system exhibiting similar overpotentials, are attributed to (a) the ease of accessibility of the electrolyte into the dimeric water pocket and (b) ultrasonic pulverization leading to an enlarged surface-to-volume ratio during the higher density of accessible active sites, both of which favor the greater kinetic facility of **1-soni** over **1-xtal**. While the onset of the OER is energetically similar for both systems, its subsequent kinetics is significantly favored in **1-soni**, compared to **1-xtal**. Accordingly, the TOF for **1-soni** ($18.6 \times 10^{-2}$ $s^{-1}$) is also 2.5-fold higher, compared to **1-xtal** ($7.2 \times 10^{-2}$ $s^{-1}$) (Figures 2c and 2d).

The continuous relay-structure formed by the hydrogen-bonded water network within the hydrophilic-transport channel of dimeric **1-soni** (Figure 1f) plays a decisive role in achieving the high TOF and favorable Tafel slope (Figure 2c−f). In fact, the TOF achieved for **1-soni** is significantly higher than those estimated in several other reports utilizing heterogeneous catalysts in nanostructured or molecular forms (Table S5).[56−58] This presents an important finding in the context of heterogeneous OER, where the majority of the studies have focused on the creation of active sites with controlled density and stability while side-stepping the tuning of its chemical environment to enable better access and coordination of the electroactive species.[59,60]

Having established the intrinsically higher activity of **1-soni**, we were enticed by the prospect of leveraging its magnetic property to further enhance the kinetics of OER. We note that, although magneto-electrocatalysis has been receiving renewed interest since the work of Pineda et al., the range of materials investigated have been restricted to nanostructured materials, coatings, and bulk-scale systems.[36,40,61] Therefore, our strategy seeks to synergistically combine the diverse disciplines of precisely crafted ligand fields in molecular systems with heterogeneous magneto-electrocatalysis.

Application of a weak magnetic field (50−300 mT) produced remarkable enhancements in their catalytic activity (Table 1, Figures 2 and 3). A significant and monotonic decrease in the OER overpotential is observed for both **1-soni** and **1-xtal** upon an increase in the strength of the externally applied magnetic field (Figures 2a and 2b). Given the near-identical geometries of both **1-xtal** and **1-soni**, the quantitative magneto-electrocatalytic lowering of overpotential is similar in both of these systems (25% for **1-xtal** and 28% for **1-soni** at 300 mT). Similar to the large difference in Tafel slopes observed without a magnetic field, the overall kinetic enhancements obtained in the presence of an external magnetic field (300 mT) are significantly larger for **1-soni** (56%), compared to **1-xtal** (46%) (Table 1, Figures 2c and 2d). Such a behavior, with **1-soni** dominating the OER energetics both at 0 and 300 mT reaffirms our understanding of the secondary coordination sphere playing an important role in controlling the OER kinetics (vide supra). Following these, the TOF undergoes an unprecedented enhancement of 134% (from $18.6 \times 10^{-2}$ $s^{-1}$ to $43.7 \times 10^{-2}$ $s^{-1}$) in the case of **1-soni** (Figure 2d). Concurrently, a similar enhancement with a lower magnitude (67%) is observed with **1-xtal**, again validating our

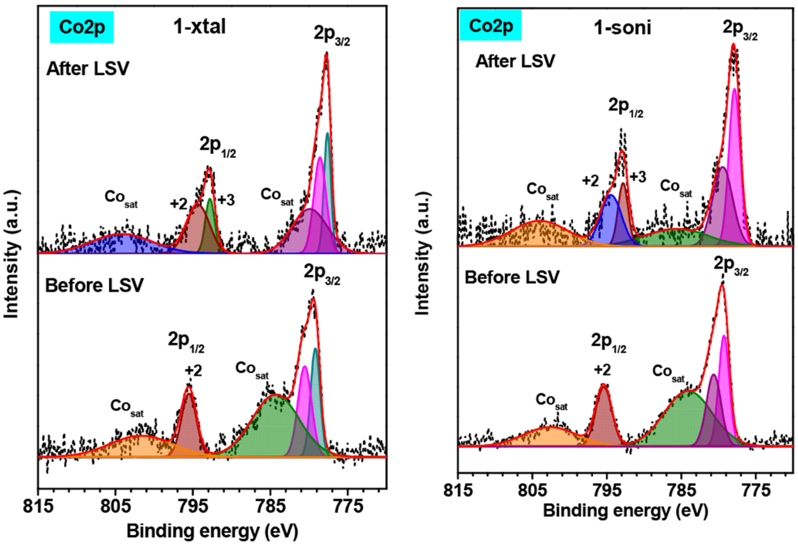

**Figure 4. X-ray photoelectron spectroscopy (XPS) of (a) 1-xtal and (b) 1-soni before and after the chronoamperometric stability evolution.**

predictions (Figure 2c). Such large enhancements in TOF, corresponding to the lowering of overpotential, are consistent with Butler−Volmer kinetics and form one of the highest TOF estimates in molecular electrocatalytic systems of heterogeneous nature.

The pronounced effect of the coordination environment is further amplified in the Nyquist plot, which exhibits a clear trend in the charge transfer resistance ($R_{ct}$) for the two systems (Figures 3a and 3b). The $R_{ct}$ of **1-xtal** (257 Ω) is significantly higher than that of **1-soni** (155 Ω) in the absence of an external magnetic field. While the hydrogen-bonded methanol-incorporated environment in **1-xtal** impedes the charge transfer across the interface, variant **1-soni** exhibits lower $R_{ct}$ aided by the extensive dimeric water pocket (Figure 3c and 3d, Figure 1f). The hydrogen-bonded water network favors the proton-coupled electron transfer pathway in **1-soni**, while being less effective in **1-xtal**. Thus, the first coordinated water pocket and the extended hydrogen-bonded network facilitated by the phosphates present a synergistic combination to lower $R_{ct}$ in **1-soni**, compared to **1-xtal** (Figure 3a−d). Consistent with our earlier experimental results (Figure 2, Table 1), the double-layer capacitance ($C_{dl}$) exhibits proportional changes with the introduction of an external magnetic field (Figure 3a−d). While $R_{ct}$ reduces by 41% (from 155 Ω to 91 Ω) for **1-soni**, the quantitative decrease is from 257 Ω to 194 Ω for **1-xtal**. Correspondingly, $C_{dl}$ also increases by 88% for **1-soni** and by 67% for **1-xtal** (Figures 3c and 3d). The magnitude of these changes concurs with the observed kinetic enhancements through the Tafel slope and TOF (Figure 2c−f, Table 1). Taken together, all of these results exclusively underline the role of configuring the water transport pathways to the active site and further boosting it through an externally applied magnetic field (Figure S12). Finally, the long-term stability of these catalysts is established by continuous chronoamperometry at 14.5 mA/cm$^2$ in the presence of 300 mT of an external magnetic field with **1-soni**. The catalysts exhibit unchanged activity for over 28 h (100 800 s; see Figures 3e and 3f for **1-soni**, and Figure S13 for **1-xtal**), as reinforced from identical LSVs recorded before and after the stability tests. The stability of both the catalytic systems is evident from the chronoamperometric studies, which is further confirmed through X-ray photoelectron spectroscopy (XPS) (Figure 4).[62,63] The spectra of pristine **1-xtal** and **1-soni** exhibit clear features corresponding to 779.5 and 795.5 eV, arising from spin-orbit-coupled $2p_{3/2}$ and $2p_{1/2}$, respectively. Furthermore, the Co$^{2+}$ features in both **1-xtal** and **1-soni**, along with the associated shakeup satellites (783.9 and 802.7 eV) are completely retained, along with the emergence of additional peaks corresponding to Co$^{3+}$ (792.7 eV) after the chronoamperometric experiments. Along with the stability of the current density in chronoamperometric runs, the invariant spectroscopic signatures thereby confirm the unchanged chemical nature of **1-xtal** (Figure S13) and **1-soni** (Figures 3e and 3f) through catalytic cycles.

One of the primary characteristics of spin-parity-driven electrocatalysis is the immediate quenching of the magneto-electrocatalytic enhancements upon removal of the external magnetic field. Therefore, in order to establish the proposed mechanism, the external magnetic field was alternated between ON and OFF states during the LSV measurements, whereupon identical ON−OFF behavior was observed in the magneto-electrocatalytic enhancements for several cycles (Figure S14). This observation precludes the dominant contribution from effects such as magnetohydrodynamic and thermomagnetics but pinpoints the change in the reaction pathway as the possible mechanism. This has been demonstrated in our earlier work[61] and in similar carbon−metal oxide interfaces,[64] in the context of spintronics-based memory devices.

To decipher the role of the secondary sphere and the effect of the magnetic field, density functional theory (DFT) calculations were carried out (from which Scheme S2 is postulated). For this catalytic process, the rate-limiting step of O−O bond formation was considered from the putative Co(III)−O$^{\bullet}$ (alternatively Co(IV)═O) species that eventually leads to formation of Co(III)−OOH species.[65,66] Three spin states have been considered for the Co(III)−O$^{\bullet}$ species of **1-xtal**: $S$ = 5/2, 3/2, and 1/2. Of these spin states, our calculations reveal that $S = {}^{1}/_{2}$ is the ground state ($^{2}\mathbf{R}_{ls}$; see the computational details for a description, as well as Figure 5 and Figures S15−S17). The ground state has $(d_{xy})^2(d_{xz})^2(d_{yz})^1(d_{x^2-y^2})^0(d_{z^2})^0$ electronic configuration (see Figure S16) with unpaired electron expected on the $d_{yz}$ orbital. However, the $d_{xz}$ orbital is closely lying, suggesting near

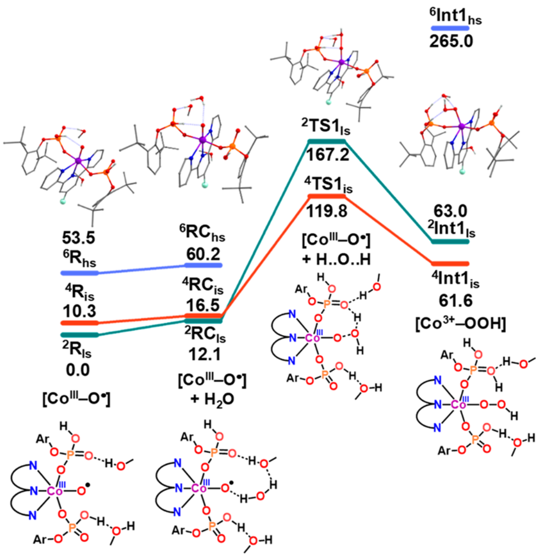

**Figure 5. Energy profile diagram for the proposed mechanism, containing solvent-free energies (ΔG) at the B3LYP-D3/def2-TZVP level of theory, for the water oxidation process proceeding through Co(III)−O• in 1-xtal.**

degeneracy. The Wiberg bond index (WBI) for the Co−O bond of the $^2$**R**$_{ls}$ species is 0.84, indicating the single-bond character (Table S6). This suggests a Co(III)−O• character rather than a pure Co(IV)═O species, consistent with the species expected based on oxo-wall theory.[67−70] The computed Co−O bond length (1.797 Å), the spin density plot, and the $\nu$(Co−O) stretching frequency (560 cm$^{-1}$) affirm this electronic structure (see Figure S15 and Tables S7 and S8).[70−72] The other two spin states, viz. quartet ($^4$**R**$_{is}$) and sextet ($^6$**R**$_{hs}$), were determined to be energetically higher by 10.3 and 53.3 kJ/mol, respectively. The low-lying $S = {}^3/_2$ state is due to the near degeneracy of the $d_{xz}/d_{yx}$ orbitals. An insignificant doublet−quartet gap suggests the possible participation of both states in the O−O bond formation.

Subsequently, the approach of a water molecule to the Co(III)-O• moiety results in the formation of a reactant complex that demonstrates robust O1w···H1w hydrogen bonding interaction, as substantiated by the bond distance of 1.893 Å (Figures S18−S20 and Table S8). The formation of this complex is endothermic with an $S = {}^1/_2$ ground state ($^2$**RC**$_{ls}$; see Figure 5). At this level, the doublet and quartet gap is reduced to 4.4 kJ/mol (Δ$E$ = $^4$**RC**$_{is}$ − $^2$**RC**$_{ls}$), suggesting the stability of the quartet state upon the approach of a water molecule. This small gap clearly indicates the contribution of both states to the reactivity. Furthermore, the application of a small magnetic field drives the spin-state switching between the proximal $S = {}^3/_2$ and ${}^1/_2$ states. Furthermore, the eigenvalue plot revealed a smaller HOMO−LUMO gap for the $^2$**RC**$_{ls}$ state of the reactant complex, compared to the $^2$**R**$_{ls}$ state of the reactant species (see Figures S19 and S20). In the next step, the formation of the O−O bond via the transition state (**TS1**) is assumed (Figure S21). In the context of the transition state, the quartet state ($^4$**TS1**$_{is}$) emerges as the lowest-lying state with an estimated energy barrier of 119.8 kJ/mol, relative to the doublet $^2$**R**$_{ls}$ state. On the other hand, the $^2$**TS**$_{ls}$ state is found to have a much steeper kinetic barrier (167.2 kJ/mol). The presence of the secondary coordination sphere in **1-xtal** along with the additional water molecules located in the vicinity of the Co(II) facilitates activation of water by inducing total elongation by ∼0.3 Å of the H1w−O2w bond (Figure S21). This elongation arises due to the hydrogen bonding interaction between the oxygen atom (O12) of the phosphate and the water molecule. The transition state $^4$**TS1**$_{is}$ displays O−O bond formation with a distance of 1.806 Å, consistent with earlier reports.[73]

The NBO and WBI analysis of the quartet species shows single bond character in Co(III)−O• species, along with a partial single bond character between the O1w−O2w bond. The subsequent activation of the Ow2−H1a bond in the second water molecule is synonymous with the O−O bond formation step (Figures S21−S25, and Tables S9−S19). The SNO analysis revealed this to be a hydrogen atom transfer reaction (Figure S26). A spin crossover phenomenon is observed during the transition from the reactant complex to the transition state, specifically from the doublet $^2$**RC**$_{ls}$ state to the quartet $^4$**TS**$_{is}$ state. This demands a minimum energy crossing point between the two surfaces prior to the transition state.[74,75] However, if a magnetic field is applied, the $S = {}^3/_2$ state is expected to be stabilized as a ground state and can thus entirely avoid the minimum energy crossing point (MECP), leading to a faster reaction. As shown earlier in the two-state reactivity concept, the MECP is strongly correlated to spin−orbit coupling and thus can have steep energy requirements. As the application of a magnetic field completely eliminates this possibility, by stabilizing the $S = {}^3/_2$ as the ground state, the reaction proceeds entirely on the quartet surface, leading to faster kinetics, which is consistent with the experimental observations.[76] In the final step, the formation of the Co(III)−OOH ($^4$**Int1**$_{is}$) species is expected, where $S = {}^3/_2$ is determined to be the ground state. This step is endothermic by 61.6 kJ/mol (Figure S27). The net result is a small energy difference between the doublet and quartet at the RC level and a comparatively large energy difference (47.4 kJ/mol) at the transition state. This makes this complex an apt example to showcase how application of a weak magnetic field drives significant alteration of the entire energy landscape. In addition, the $S = {}^3/_2$ Co(III)−OOH species also has a greater tendency to release oxygen (with a triplet ground state), suggesting a feasible OER pathway.

In summary, a cobalt phosphate complex, in two different physical states (single crystalline **1-xtal** and pulverized **1-soni**), has been demonstrated to show significant water oxidation capability, due to its unique ligand field environment. The existence of phosphoryl P═O and P−OH groups, along with coordinated and lattice water molecules, leads to the formation of a hydrophilic channel and, hence, a *Janus* face. This ligand-directed supramolecular assembly formation facilitates the title compound to be an efficient water oxidation heterogeneous electrocatalyst. It has further been established that the application of an optimum 300 mT magnetic field significantly increases the OER catalytic efficiency. Detailed DFT calculations suggest that the catalytically active species has two close-lying doublet and quartet states with latter, that is accessed through application of an external magnetic field, having a substantially lower kinetic barrier for O−O bond formation. The calculations have further revealed this spin-state switching phenomenon to be primarily responsible for significantly lowering the kinetic barrier for the O−O bond formation. The stabilization of the quartet state as the ground state at the applied magnetic field rationalizes the enhanced OER observation, an unprecedented observation for molecular catalysts on electrode surfaces, signifying a potential confluence of principles of single molecular magnetism with the design principles of electrocatalysts.

## ■ ASSOCIATED CONTENT

### Supporting Information

The Supporting Information is available free of charge at https://pubs.acs.org/doi/10.1021/acsmaterialslett.4c00763.

Additional figures and tables, crystallographic details, spectral characterization, and computational details (PDF)

Crystallographic data (CIF)

## ■ AUTHOR INFORMATION

### Corresponding Authors

**Ramaswamy Murugavel** − *Department of Chemistry, Indian Institute of Technology Bombay, Mumbai 400076, India;* orcid.org/0000-0002-1816-3225; Email: rmv@chem.iitb.ac.in

**Chandramouli Subramaniam** − *Department of Chemistry, Indian Institute of Technology Bombay, Mumbai 400076, India;* orcid.org/0000-0001-8335-7395; Email: csubbu@chem.iitb.ac.in

**Gopalan Rajaraman** − *Department of Chemistry, Indian Institute of Technology Bombay, Mumbai 400076, India;* orcid.org/0000-0001-6133-3026; Email: rajaraman@chem.iitb.ac.in

### Authors

**Tulasi Prapakaran** − *Department of Chemistry, Indian Institute of Technology Bombay, Mumbai 400076, India*

**Ananya Chowdhury** − *Department of Chemistry, Indian Institute of Technology Bombay, Mumbai 400076, India*

**Sunita Sharma** − *Department of Chemistry, Indian Institute of Technology Bombay, Mumbai 400076, India*

**Itisha Dwivedi** − *Department of Chemistry, Indian Institute of Technology Bombay, Mumbai 400076, India*

Complete contact information is available at: https://pubs.acs.org/10.1021/acsmaterialslett.4c00763

### Author Contributions

$^{\nabla}$A. Chowdhury and S. Sharma contributed equally to this work.

### Notes

The authors declare no competing financial interest.

## ■ ACKNOWLEDGMENTS

This work was supported by SERB, New Delhi (Nos. EMR/2017/002767, CRG/2022/002406, and SB/S2/JCB-85/2014 to R.M., No. SB/SJF/2021-22/07, and DO/2023-HSBC001-002 to C.S.; Nos. SB/SJF/2019-20/12 and CRG/2022/001697 to G.R.) We thank SAIF IITB, IITB-HPC, and other central facilities for various characterization data and computational studies.

## ■ DEDICATION

This work is dedicated to Prof. M. S. Balakrishna on the occasion of his 65th birthday.

## ■ REFERENCES

(1) De Luna, P.; Hahn, C.; Higgins, D.; Jaffer, S. A.; Jaramillo, T. F.; Sargent, E. H. What would it take for renewably powered electrosynthesis to displace petrochemical processes? *Science* **2019**, *364*, eaav3506.

(2) Yu, F.; Zhou, H.; Huang, Y.; Sun, J.; Qin, F.; Bao, J.; Goddard, W. A.; Chen, S.; Ren, Z. High-performance bifunctional porous non-noble metal phosphide catalyst for overall water splitting. *Nat. Commun.* **2018**, *9*, 2551.

(3) Walter, M. G.; Warren, E. L.; McKone, J. R.; Boettcher, S. W.; Mi, Q.; Santori, E. A.; Lewis, N. S. Solar Water Splitting Cells. *Chem. Rev.* **2010**, *110*, 6446−6473.

(4) Turner, J. A. Sustainable Hydrogen Production. *Science* **2004**, *305*, 972−974.

(5) Lee, Y.; Suntivich, J.; May, K. J.; Perry, E. E.; Shao-Horn, Y. Synthesis and Activities of Rutile $IrO_2$ and $RuO_2$ Nanoparticles for Oxygen Evolution in Acid and Alkaline Solutions. *J. Phys. Chem. Lett.* **2012**, *3*, 399−404.

(6) Rossmeisl, J.; Qu, Z. W.; Zhu, H.; Kroes, G. J.; Nørskov, J. K. Electrolysis of water on oxide surfaces. *J. Electroanal. Chem.* **2007**, *607*, 83−89.

(7) Li, J.; Triana, C. A.; Wan, W.; Adiyeri Saseendran, D. P.; Zhao, Y.; Balaghi, S. E.; Heidari, S.; Patzke, G. R. Molecular and heterogeneous water oxidation catalysts: recent progress and joint perspectives. *Chem. Soc. Rev.* **2021**, *50*, 2444−2485.

(8) Tang, C.; Cheng, N.; Pu, Z.; Xing, W.; Sun, X. NiSe Nanowire Film Supported on Nickel Foam: An Efficient and Stable 3D Bifunctional Electrode for Full Water Splitting. *Angew. Chem., Int. Ed.* **2015**, *54*, 9351−9355.

(9) Lee, S. W.; Carlton, C.; Risch, M.; Surendranath, Y.; Chen, S.; Furutsuki, S.; Yamada, A.; Nocera, D. G.; Shao-Horn, Y. The Nature of Lithium Battery Materials under Oxygen Evolution Reaction Conditions. *J. Am. Chem. Soc.* **2012**, *134*, 16959−16962.

(10) Kanan, M. W.; Nocera, D. G. In Situ Formation of an Oxygen-Evolving Catalyst in Neutral Water Containing Phosphate and $Co^{2+}$. *Science* **2008**, *321*, 1072−1075.

(11) Long, X.; Li, J.; Xiao, S.; Yan, K.; Wang, Z.; Chen, H.; Yang, S. A Strongly Coupled Graphene and FeNi Double Hydroxide Hybrid as an Excellent Electrocatalyst for the Oxygen Evolution Reaction. *Angew. Chem., Int. Ed.* **2014**, *53*, 7584−7588.

(12) Jung, J.-I.; Jeong, H. Y.; Lee, J.-S.; Kim, M. G.; Cho, J. A Bifunctional Perovskite Catalyst for Oxygen Reduction and Evolution. *Angew. Chem., Int. Ed.* **2014**, *53*, 4582−4586.

(13) Xu, K.; Chen, P.; Li, X.; Tong, Y.; Ding, H.; Wu, X.; Chu, W.; Peng, Z.; Wu, C.; Xie, Y. Metallic Nickel Nitride Nanosheets Realizing Enhanced Electrochemical Water Oxidation. *J. Am. Chem. Soc.* **2015**, *137*, 4119−4125.

(14) Sun, H.; Yan, Z.; Liu, F.; Xu, W.; Cheng, F.; Chen, J. Self-Supported Transition-Metal-Based Electrocatalysts for Hydrogen and Oxygen Evolution. *Adv. Mater.* **2020**, *32*, 1806326.

(15) Blakemore, J. D.; Crabtree, R. H.; Brudvig, G. W. Molecular Catalysts for Water Oxidation. *Chem. Rev.* **2015**, *115*, 12974−13005.

(16) Matheu, R.; Garrido-Barros, P.; Gil-Sepulcre, M.; Ertem, M. Z.; Sala, X.; Gimbert-Suriñach, C.; Llobet, A. The development of molecular water oxidation catalysts. *Nat. Rev. Chem.* **2019**, *3*, 331−341.

(17) Garrido-Barros, P.; Gimbert-Suriñach, C.; Matheu, R.; Sala, X.; Llobet, A. How to make an efficient and robust molecular catalyst for water oxidation. *Chem. Soc. Rev.* **2017**, *46*, 6088−6098.

(18) Kärkäs, M. D.; Verho, O.; Johnston, E. V.; Åkermark, B. Artificial Photosynthesis: Molecular Systems for Catalytic Water Oxidation. *Chem. Rev.* **2014**, *114*, 11863−12001.

(19) Artero, V.; Chavarot-Kerlidou, M.; Fontecave, M. Splitting Water with Cobalt. *Angew. Chem., Int. Ed.* **2011**, *50*, 7238−7266.

(20) Zhang, X.; Zhu, K.; Xie, C.; Yang, P. Vertically implanting $MoSe_2$ nanosheets on superior thin C-doped g-$C_3N_4$ nanosheets towards interface-enhanced electrochemical activities. *Carbon* **2024**, *220*, 118884.

(21) Zhang, X.; Yang, P.; Chen, H. S.; Jiang, S. P. Carbon layer derived carrier transport in Co/g-$C_3N_4$ nanosheet junctions for efficient $H_2O_2$ production and NO removal. *Chem. Eng. J.* **2024**, *479*, 147609.

(22) Zhang, X.; Chen, H. S.; Jiang, S. P.; Yang, P. $W_{18}O_{49}$/crystalline g-$C_3N_4$ layered heterostructures with full solar energy harvesting towards efficient $H_2O_2$ generation and NO conversion. *Nano Energy* **2024**, *120*, 109160.

(23) Zhang, X.; Yang, P.; Jiang, S. P. NiCo-layered double hydroxide/g-$C_3N_4$ heterostructures with enhanced adsorption capacity and photoreduction of Cr(VI). *Appl. Surf. Sci.* **2021**, *556*, 149772.

(24) Saha, J.; Verma, S.; Ball, R.; Subramaniam, C.; Murugavel, R. Compositional Control as the Key for Achieving Highly Efficient OER Electrocatalysis with Cobalt Phosphates Decorated Nanocarbon Florets. *Small* **2020**, *16*, 1903334.

(25) Pothiraja, R.; Sathiyendiran, M.; Butcher, R. J.; Murugavel, R. Cobalt and Manganese Nets via Their Wires: Facile Transformation in Metal−Diorganophosphates. *Inorg. Chem.* **2004**, *43*, 7585−7587.

(26) Sathiyendiran, M.; Murugavel, R. Di-*tert*-butyl Phosphate as Synthon for Metal Phosphate Materials via Single-Source Coordination Polymers $[M(dtbp)_2]_n$ (M = Mn, Cu) and $[Cd(dtbp)_2(H_2O)]_n$ (dtbp-H = $(t\text{BuO})_2P(O)OH$). *Inorg. Chem.* **2002**, *41*, 6404−6411.

(27) Borah, A.; Saha, J.; Sharma, S.; Chaudhary, S.; Gupta, S. K.; Rajaraman, G.; Subramaniam, C.; Murugavel, R. Ligand-Field Directed Electronic Effects in Heterogenized Bifunctional Co(II) Molecular Clusters Accomplish Efficient Overall Water Splitting. *ACS Catal.* **2023**, *13*, 8535−8550.

(28) Dogutan, D. K.; McGuire, R., Jr; Nocera, D. G. Electocatalytic Water Oxidation by Cobalt(III) Hangman *β*-Octafluoro Corroles. *J. Am. Chem. Soc.* **2011**, *133*, 9178−9180.

(29) Wang, J.; Dou, S.; Wang, X. Structural tuning of heterogeneous molecular catalysts for electrochemical energy conversion. *Sci. Adv.* **2021**, *7*, eabf3989.

(30) Xie, C.; Niu, Z.; Kim, D.; Li, M.; Yang, P. Surface and Interface Control in Nanoparticle Catalysis. *Chem. Rev.* **2020**, *120*, 1184−1249.

(31) Wang, J.; Ge, X.; Liu, Z.; Thia, L.; Yan, Y.; Xiao, W.; Wang, X. Heterogeneous Electrocatalyst with Molecular Cobalt Ions Serving as the Center of Active Sites. *J. Am. Chem. Soc.* **2017**, *139*, 1878−1884.

(32) Blakemore, J. D.; Gupta, A.; Warren, J. J.; Brunschwig, B. S.; Gray, H. B. Noncovalent Immobilization of Electrocatalysts on Carbon Electrodes for Fuel Production. *J. Am. Chem. Soc.* **2013**, *135*, 18288−18291.

(33) Jackson, M. N.; Oh, S.; Kaminsky, C. J.; Chu, S. B.; Zhang, G.; Miller, J. T.; Surendranath, Y. Strong Electronic Coupling of Molecular Sites to Graphitic Electrodes via Pyrazine Conjugation. *J. Am. Chem. Soc.* **2018**, *140*, 1004−1010.

(34) Jiao, Y.; Zheng, Y.; Jaroniec, M.; Qiao, S. Z. Design of electrocatalysts for oxygen- and hydrogen-involving energy conversion reactions. *Chem. Soc. Rev.* **2015**, *44*, 2060−2086.

(35) Bullock, R. M.; Das, A. K.; Appel, A. M. Surface Immobilization of Molecular Electrocatalysts for Energy Conversion. *Chem.—Eur. J.* **2017**, *23*, 7626−7641.

(36) Garcés-Pineda, F. A.; Blasco-Ahicart, M.; Nieto-Castro, D.; López, N.; Galán-Mascarós, J. R. Direct magnetic enhancement of electrocatalytic water oxidation in alkaline media. *Nat. Energy* **2019**, *4*, 519−525.

(37) Gracia, J. Spin dependent interactions catalyse the oxygen electrochemistry. *Phys. Chem. Chem. Phys.* **2017**, *19*, 20451−20456.

(38) Gracia, J.; Sharpe, R.; Munarriz, J. Principles determining the activity of magnetic oxides for electron transfer reactions. *J. Catal.* **2018**, *361*, 331−338.

(39) Fahidy, T. Z. An MHD-based treatment of electrolysis in magnetic fields generated inside a solenoid. *J. Appl. Electrochem.* **2002**, *32*, 551−559.

(40) Zhang, Y.; Liang, C.; Wu, J.; Liu, H.; Zhang, B.; Jiang, Z.; Li, S.; Xu, P. Recent Advances in Magnetic Field-Enhanced Electrocatalysis. *ACS Appl. Energy Mater.* **2020**, *3*, 10303−10316.

(41) Luo, S.; Elouarzaki, K.; Xu, Z. J. Electrochemistry in Magnetic Fields. *Angew. Chem., Int. Ed.* **2022**, *61*, No. e202203564.

(42) Ge, J.; Chen, R. R.; Ren, X.; Liu, J.; Ong, S. J. H.; Xu, Z. J. Ferromagnetic−Antiferromagnetic Coupling Core−Shell Nanoparticles with Spin Conservation for Water Oxidation. *Adv. Mater.* **2021**, *33*, 2101091.

(43) Chen, R. R.; Chen, G.; Ren, X.; Ge, J.; Ong, S. J. H.; Xi, S.; Wang, X.; Xu, Z. J. $SmCo_5$ with a Reconstructed Oxyhydroxide Surface for Spin-Selective Water Oxidation at Elevated Temperature. *Angew. Chem., Int. Ed.* **2021**, *60*, 25884−25890.

(44) Wu, T.; Ren, X.; Sun, Y.; Sun, S.; Xian, G.; Scherer, G. G.; Fisher, A. C.; Mandler, D.; Ager, J. W.; Grimaud, A.; Wang, J.; Shen, C.; Yang, H.; Gracia, J.; Gao, H.-J.; Xu, Z. J. Spin pinning effect to reconstructed oxyhydroxide layer on ferromagnetic oxides for enhanced water oxidation. *Nat. Commun.* **2021**, *12*, 3634.

(45) Li, Z.; Wang, Z.; Xi, S.; Zhao, X.; Sun, T.; Li, J.; Yu, W.; Xu, H.; Herng, T. S.; Hai, X.; Lyu, P.; Zhao, M.; Pennycook, S. J.; Ding, J.; Xiao, H.; Lu, J. Tuning the Spin Density of Cobalt Single-Atom Catalysts for Efficient Oxygen Evolution. *ACS Nano* **2021**, *15*, 7105−7113.

(46) Zhou, G.; Wang, P.; Li, H.; Hu, B.; Sun, Y.; Huang, R.; Liu, L. Spin-state reconfiguration induced by alternating magnetic field for efficient oxygen evolution reaction. *Nat. Commun.* **2021**, *12*, 4827.

(47) Saini, K.; Nair, A. N.; Yadav, A.; Enriquez, L. G.; Pollock, C. J.; House, S. D.; Yang, S.; Guo, X.; Sreenivasan, S. T. Nickel-Based Single-Molecule Catalysts with Synergistic Geometric Transition and Magnetic Field-Assisted Spin Selection Outperform $RuO_2$ for Oxygen Evolution. *Adv. Energy Mater.* **2023**, *13*, 2302170.

(48) Murugavel, R.; Sathiyendiran, M.; Pothiraja, R.; Butcher, R. J. O−H Bond elongation in co-ordinated water through intramolecular P = O···H−O bonding. "Snap-shots" in phosphate ester hydrolysis. *Chem. Commun.* **2003**, 2546−2547.

(49) Nakamoto, K. Infrared and Raman Spectra of Inorganic and Coordination Compounds.. In *Handbook of Vibrational Spectroscopy*; John Wiley & Sons, Ltd., 2006.

(50) Salama, S.; Spiro, T. G. Resonance Raman spectra of cobalt (II)-imidazole complexes: analogs of the binding site of cobalt-substituted zinc proteins. *J. Am. Chem. Soc.* **1978**, *100*, 1105−1111.

(51) Llunell, M.; Casanova, D.; Cirera, J.; Alemany, P.; Alvarez, S. *SHAPE*; Universitat de Barcelona, Barcelona, Spain, 2013.

(52) Bhat, G. A.; Rajendran, A.; Murugavel, R. Dinuclear Manganese(II), Cobalt(II), and Nickel(II) Aryl Phosphates Incorporating 4′-Chloro-2,2′:6′,2″-Terpyridine Coligands − Efficient Catalysts for Alcohol Oxidation. *Eur. J. Inorg. Chem.* **2018**, *2018*, 795−804.

(53) Holder, C. F.; Schaak, R. E. Tutorial on Powder X-ray Diffraction for Characterizing Nanoscale Materials. *ACS Nano* **2019**, *13*, 7359−7365.

(54) Marinov, A. D.; Bravo Priegue, L.; Shah, A. R.; Miller, T. S.; Howard, C. A.; Hinds, G.; Shearing, P. R.; Cullen, P. L.; Brett, D. J. L. Ex Situ Characterization of 1T/2H $MoS_2$ and Their Carbon Composites for Energy Applications, a Review. *ACS Nano* **2023**, *17*, 5163−5186.

(55) Saha, J.; Ball, R.; Sah, A.; Kalyani, V.; Subramaniam, C. The mechanistic role of a support−catalyst interface in electrocatalytic water reduction by $Co_3O_4$ supported nanocarbon florets. *Nanoscale* **2019**, *11*, 13532−13540.

(56) Burke, M. S.; Kast, M. G.; Trotochaud, L.; Smith, A. M.; Boettcher, S. W. Cobalt−Iron (Oxy)hydroxide Oxygen Evolution Electrocatalysts: The Role of Structure and Composition on Activity, Stability, and Mechanism. *J. Am. Chem. Soc.* **2015**, *137*, 3638−3648.

(57) Locke, E.; Jiang, S.; Beaumont, S. K. Catalysis of the Oxygen Evolution Reaction by 4−10 nm Cobalt Nanoparticles. *Top. Catal.* **2018**, *61*, 977−985.

(58) Aljabour, A.; Awada, H.; Song, L.; Sun, H.; Offenthaler, S.; Yari, F.; Bechmann, M.; Scharber, M. C.; Schöfberger, W. A Bifunctional Electrocatalyst for OER and ORR based on a Cobalt(II) Triazole Pyridine Bis-[Cobalt(III) Corrole] Complex. *Angew. Chem., Int. Ed.* **2023**, *62*, No. e202302208.

(59) Roy, K. S.; Subramaniam, C.; Panchakarla, L. S. Non-Stoichiometry Induced Exsolution of Metal Oxide Nanoparticles via Formation of Wavy Surfaces and their Enhanced Electrocatalytic Activity: Case of Misfit Calcium Cobalt Oxide. *ACS Appl. Mater. Interfaces* **2021**, *13*, 9897−9907.

(60) Han, L.; Dong, S.; Wang, E. Transition-Metal (Co, Ni, and Fe)-Based Electrocatalysts for the Water Oxidation Reaction. *Adv. Mater.* **2016**, *28*, 9266−9291.

(61) Saha, J.; Ball, R.; Subramaniam, C. Premagnetized Carbon-Catalyst Interface Delivering 650% Enhancement in Electrocatalytic Kinetics of Hydrogen Evolution Reaction. *ACS Sustainable Chem. Eng.* **2021**, *9*, 7792−7802.

(62) McIntyre, N. S.; Cook, M. G. X-ray photoelectron studies on some oxides and hydroxides of cobalt, nickel, and copper. *Anal. Chem.* **1975**, *47*, 2208−2213.

(63) García-López, V.; Giaconi, N.; Poggini, L.; Calbo, J.; Juhin, A.; Cortigiani, B.; Herrero-Martín, J.; Ortí, E.; Mannini, M.; Clemente-León, M.; Coronado, E. Spin-Crossover Grafted Monolayer of a Co(II) Terpyridine Derivative Functionalized with Carboxylic Acid Groups. *Adv. Funct. Mater.* **2023**, *33*, 2300351.

(64) Moorsom, T.; Rogers, M.; Scivetti, I.; Bandaru, S.; Teobaldi, G.; Valvidares, M.; Flokstra, M.; Lee, S.; Stewart, R.; Prokscha, T.; et al. Reversible spin storage in metal oxide—fullerene heterojunctions. *Sci. Adv.* **2020**, *6*, eaax1085.

(65) Nguyen, A. I.; Ziegler, M. S.; Oña-Burgos, P.; Sturzbecher-Hohne, M.; Kim, W.; Bellone, D. E.; Tilley, T. D. Mechanistic Investigations of Water Oxidation by a Molecular Cobalt Oxide Analogue: Evidence for a Highly Oxidized Intermediate and Exclusive Terminal Oxo Participation. *J. Am. Chem. Soc.* **2015**, *137*, 12865−12872.

(66) Zhang, M.; Frei, H. Towards a Molecular Level Understanding of the Multi-Electron Catalysis of Water Oxidation on Metal Oxide Surfaces. *Catal. Lett.* **2015**, *145*, 420−435.

(67) Ballhausen, C. J.; Gray, H. B. The electronic structure of the vanadyl ion. *Inorg. Chem.* **1962**, *1*, 111−122.

(68) Gray, H. B.; Winkler, J. R. Living with Oxygen. *Acc. Chem. Res.* **2018**, *51*, 1850−1857.

(69) Gray, H. B. Elements of Life at the Oxo Wall. *Chem. Int.* **2019**, *41*, 16−19.

(70) Sen, A.; Rajaraman, G. Can you break the oxo-wall? A multiconfigurational perspective. *Faraday Discuss.* **2022**, *234*, 175−194.

(71) Andris, E.; Navrátil, R.; Jašík, J.; Srnec, M.; Rodríguez, M.; Costas, M.; Roithová, J. M−O Bonding Beyond the Oxo Wall: Spectroscopy and Reactivity of Cobalt(III)-Oxyl and Cobalt(III)-Oxo Complexes. *Angew. Chem., Int. Ed.* **2019**, *58*, 9619−9624.

(72) Wang, B.; Lee, Y.-M.; Tcho, W.-Y.; Tussupbayev, S.; Kim, S.-T.; Kim, Y.; Seo, M. S.; Cho, K.-B.; Dede, Y.; Keegan, B. C.; Ogura, T.; Kim, S. H.; Ohta, T.; Baik, M.-H.; Ray, K.; Shearer, J.; Nam, W. Synthesis and reactivity of a mononuclear non-haem cobalt(IV)-oxo complex. *Nat. Commun.* **2017**, *8*, 14839.

(73) Shi, J.; Guo, Y.-H.; Xie, F.; Chen, Q.-F.; Zhang, M.-T. Redox-Active Ligand Assisted Catalytic Water Oxidation by a $\mathrm{Ru^{IV}{=}O}$ Intermediate. *Angew. Chem., Int. Ed.* **2020**, *59*, 4000−4008.

(74) Harvey, J. N.; Aschi, M.; Schwarz, H.; Koch, W. The singlet and triplet states of phenyl cation. A hybrid approach for locating minimum energy crossing points between non-interacting potential energy surfaces. *Theor. Chem. Acc.* **1998**, *99*, 95−99.

(75) Ricciarelli, D.; Belpassi, L.; Harvey, J. N.; Belanzoni, P. Spin-Forbidden Reactivity of Transition Metal Oxo Species: Exploring the Potential Energy Surfaces. *Chem.—Eur. J.* **2020**, *26*, 3080−3089.

(76) Huang, Q.; Xie, S.; Hao, J.; Ding, Z.; Zhang, C.; Sheng, H.; Zhao, J. Spin-Enhanced O−H Cleavage in Electrochemical Water Oxidation. *Angew. Chem., Int. Ed.* **2023**, *62*, No. e202300469.

https://doi.org/10.1021/acsmaterialslett.4c00763